Electronic supplementary information

Boosting Alkaline Hydrogen Evolution on RuO_2: Regulation of Intermediate Binding by Keggin-Type Polyoxometalates

Chang Liu [a], Faheem Abbas [a], Jiayang Shi [a], Sha Zhang [c], Yu Zhang [a], Duidui Zhang [a], Shunle Li [a], Chen Chen [b], Yongge Wei [a]**

a Department of Chemistry, Key Lab of Organic Optoelectronics and Molecular Engineering of Ministry of Education, Tsinghua University, Beijing 100084, PR China.

b Department of Chemistry, Tsinghua University, Beijing 100084, PR China.

c College of Grassland Science, Qingdao Agricultural University, Qingdao 266109, China.

** Corresponding Author E-mail:*

cchen@mail.tsinghua.edu.cn. ; yonggewei@mail.tsinghua.edu.cn.

Materials and Characterizations:

All chemicals, including solvents, were commercially available as the reagent grade from Adamas beta. IR spectrum was measured by using KBr pellets and recorded on a Perkin Elmer FT-IR spectrometer. Elemental analyses were performed by Elementar Analysensysteme GmbH (vario EL). PXRD characterization was performed on a Bruker D8 Advance X-ray diffractometer using Cu-K_α radiation ($\lambda = 1.5418$ Å). The morphology and size of the nanostructured products were characterized using a HITACHI H-7700 TEM with an accelerating voltage of 100 kV, and a FEI Tecnai G2 F20 S-Twin HRTEM operating at 200 kV. SEM, with energy dispersive X-ray spectroscopy (EDS) equipment, was performed on a LEO 1530. XPS experiments were carried out on a scanning X-ray microprobe (Quantera SXM, ULVAC-PHI, Inc.) operated at 250 kV, 55 eV with monochromated Al K_α radiation. N_2 sorption isotherms were collected on a Micromeritics Tristar 3020 II adsorption analyzer at −196 °C (77 K). The elemental composition of the materials was determined using an inductively coupled plasma emission spectrometer (ICP-OES) Jobin Yvon Ultima 2. BET-specific surface areas were calculated from adsorption data in a relative pressure range from 0.071 to 0.20. The pore size distribution was derived from the adsorption branch of the isotherms. Raman spectra were recorded using a HORIBA JY HR800 confocal Raman microscope employing an Ar-ion laser operating at 633 nm.

Electrochemical Measurements:

For the electrochemical measurements, a three-electrode system equipped with an electrochemical workstation (CHI660E, China) was used. The working electrode was fabricated by loading the as-prepared material onto conductive titanium foam, while the counter and reference electrodes were a graphite rod and an Hg/HgO electrode (in 1 M KOH). To accurately determine the mass loading of the in-situ grown catalysts, 1 cm² of the as-prepared $PMo_{10}V_2$-RuO_2/Ti electrode was completely dissolved in aqua regia and diluted to 25 mL. The ICP-OES analysis revealed measured concentrations of sample. The total active mass loading (POM+RuO_2) was calculated to be approximately 1.4 mg/cm². (PMo_{12}-RuO_2:1.43 mg; $PMo_{10}V_2$-RuO_2:1.36 mg) Consequently, to ensure a rigorous baseline for electrochemical evaluation, the commercial 20% Pt/C catalyst was drop-casted onto bare Ti foam with a precisely matched loading amount of 1.4 mg/cm².

All potentials provided in this article were standardized and converted to the RHE by using the equation: $E_{RHE} = E_{Hg/HgO} + 0.098V + 0.059 \cdot pH$, The cyclic voltammetry (CV) was performed in 1 M KOH solution at a sweep rate of 100 mV/s from -0.9 to 0.1 V *vs* Hg/HgO. The HER electrocatalytic activity of the catalyst was examined using linear sweep voltammetry (LSV) between -0.8 V to -1.4 V (versus Hg/HgO) with a scan rate of 10 mV/s. All polarization curves were corrected with 90% iR-drop compensation. Chronopotentiometry (CP) measurements were utilized to test the catalyst's durability. Additionally, the stability of the catalyst electrocatalyst was also evaluated by cycling the catalysts between -0.9 and -1.1 V (versus Hg/HgO) at a sweep rate of 100 mV/s for 10,000 cycles. By linearly fitting the plot resulting from the logarithm of current density *vs.* overpotential, Tafel slopes were obtained. From the Tafel equation, the Tafel slopes were calculated: $\eta = a * \log|j| + b$, where η is overpotential, a is the Tafel slope, j is the current density and b is the intercept. Turnover frequency can be calculated from the following equation: $TOF = JA/2Fn$, where J is the current density at an overpotential of 40 mV, A is the area of the electrode(1 cm^2), F is the Faraday constant (96,485C/mol), and n is the molar number of material deposited on the electrode.

The electrochemical accessible surface area (ECSA) was determined by: ECSA=C_{dl}/C_s, where C_{dl} is double-layer capacitance and Cs the specific capacitance of the sample. In this work, a general specific capacitance of Cs=0.04 mF/cm^2 (Applying this general value to POM composites may lead to slight deviations in the absolute ECSA value. However, the calculated ECSA values can still provide a highly reliable relative comparison of the active surface areas among the synthesized samples) was used based on typically reported values. C_{dl} was determined by the equation $C_{dl} = i_c/v$, where i_c is the charging current and v is the scan rate. A series of CV tests in the non-faradaic potential region (-0.7~-0.6V vs. Hg/HgO) with various scan rates (20, 40, 60, 80, 100 mV/s) were performed. By plotting measured i_c versus v, C_{dl} was obtained from the slopes of the linear fitting.

Computational details:

All calculations for structural relaxation, electronic, and catalytic properties were computed using the spin−polarized DFT approach through the Vienna ab initio Simulation Package (VASP).[1, 2] The interactions between ions and electrons were analyzed using the projector−augmented−wave (PAW) method.[3] The exchange−correlation was carried out through the generalized gradient approximation (GGA) of Perdew−Burke−Ernzerhof (PBE).[4-6] To incorporate van der Waals interactions between the catalytic surface and adsorbate Grimmes (D3−DFT) dispersion correction method was used.[7] The cutoff energy of 450 eV for plane waves was employed for valence electrons. For geometric optimization, tight convergence criteria were utilized until the forces on each atom decreased to 0.02 eV/e. The Brillion zone Monkhorst−Pack sample consists of 1×1×1 Γ points.[8] All electronic descriptors for the individual and heterostructures were tested including projected density of states analysis (PDOS), Bader charge (q),[9] and d−band centers (εd), were calculated at the same level of theory. A vacuum space of 20 Å was implemented in the Z direction to avoid interlayer interactions.

The free energy was calculated using the following equation:

$$G = E + G(T)$$

$$\begin{cases} U(T) = E_{ZPE} + \Delta U_{0\to T} \\ H(T) = U(T) + PV \\ G(T) = H(T) - TS \end{cases} \Rightarrow G(T) = E_{ZPE} + \Delta U_{0\to T} + PV - TS$$

where zero-point energy corrections (EZPE) could be derived after frequency calculation by:

$$E_{ZPE} = \frac{1}{2}\sum h v_i$$

G(T) can be easily calculated by vaspkit (T was set to be 25 ° C).

According to the Tafel slope value obtained in the experiment, the actual reaction mechanism follows the Volmer-Heyrovsky step:

$$* + 2H_2O + 2e^- \xrightarrow[\text{Volmer step}]{} H^* + H_2O + OH^- + e^- \xrightarrow[\text{Heyrovsky step}]{} * + 2OH^- + H_2$$

* Indicates the adsorption site. In HER equilibrium potential, the free energy before and after the reaction should be the same. Under this assumption, calculating the exact free energy of OH− in solution can be avoided by calculating the hydrogen

electrode [11]. Four stages are mainly considered in the whole calculation process:

1. Initial state
2. Adsorption of active water
3. Formation of H* intermediates;
4. H_2 formation

The free energy is calculated as:

$$G_1 = G_* + G_{H_2O}$$
$$G_2 = G_{(H-OH)^*}$$
$$G_3 = G_{H^*} + G_{OH^-}$$
$$G_4 = G_* + G_{OH^-} + 1/2\, G_{H_2}$$
$$G_1 = G_4$$

The free energy is calculated as follows:

ΔG (H2O) (ΔG (H2O) = G2 - G1) value as a descriptor Volmer step activity.

ΔG (H*) (ΔG (H*) = G3 - G4) value is as a descriptor for the Heyrovsky steps, according to the calculation results map free energy of the steps.

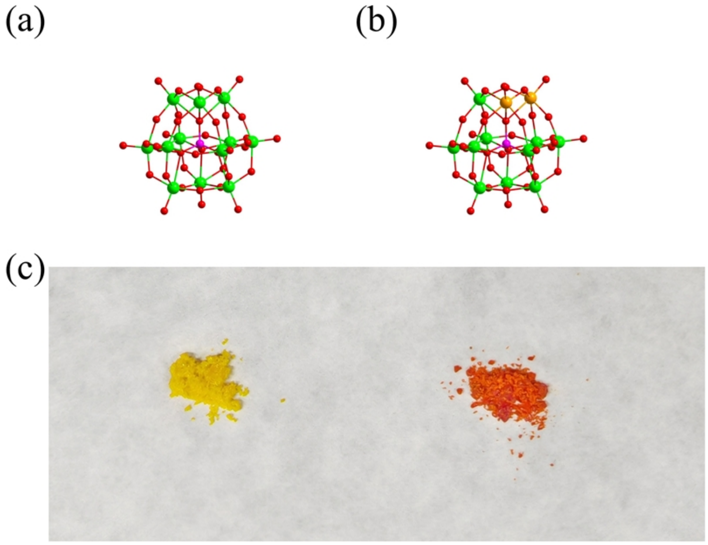

Figure S1. (a) PMo$_{12}$, (b)PMo$_{10}$V$_2$, (c) the electron micrograph of the PMo$_{12}$ and PMo$_{10}$V$_2$.

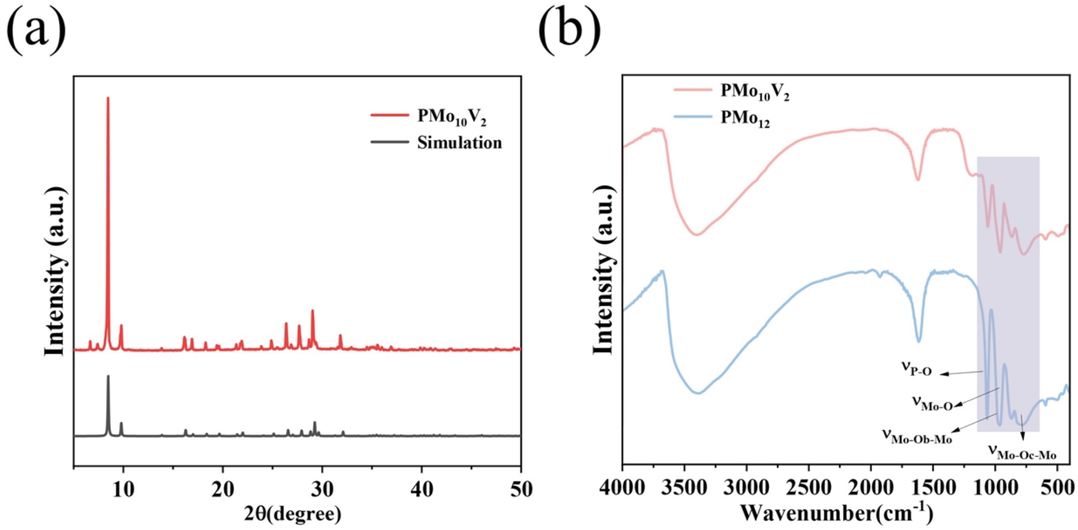

Figure S2. (a) Simulated and experimental PXRD patterns of $PMo_{10}V_2$, (b) FT-IR spectra of PMo_{12}, $PMo_{10}V_2$.

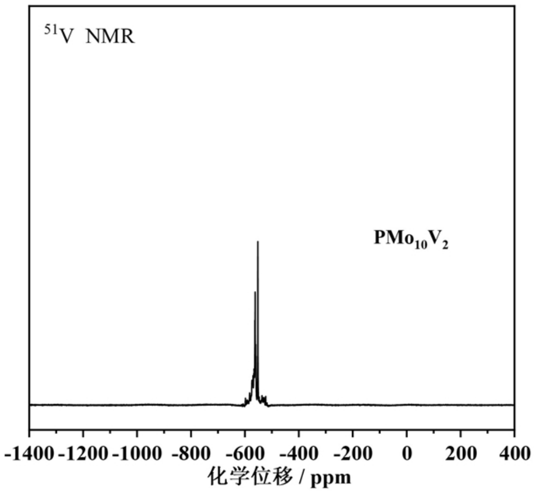

Figure S3: The ^{51}V NMR spectra of $PMo_{10}V_2$.

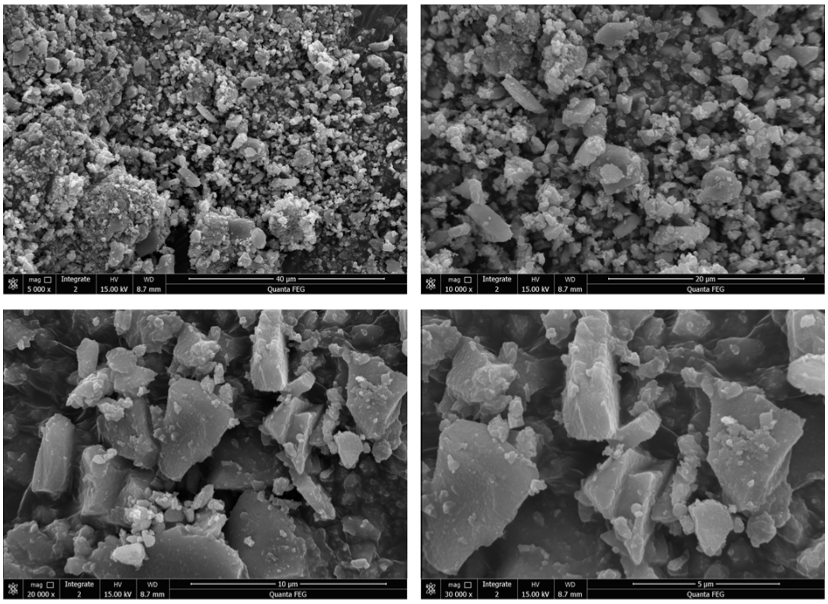

Figure S4. The SEM image of RuO_2.

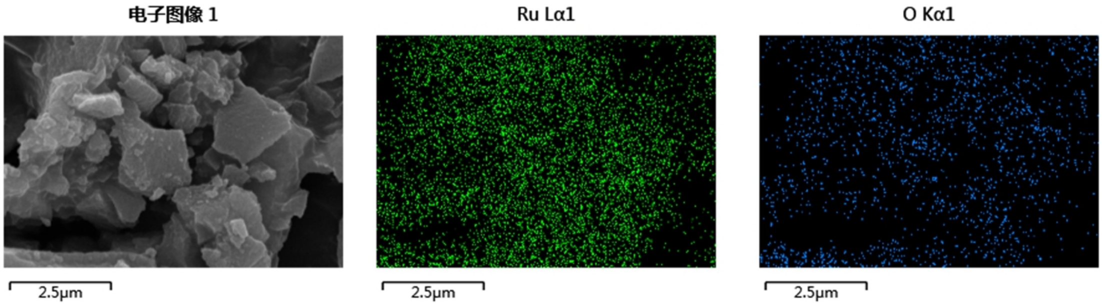

Figure S5. EDS mapping profile of RuO_2.

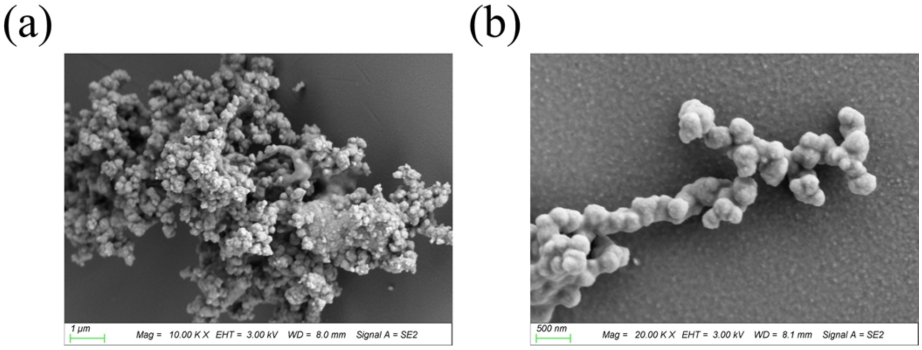

Figure S6. The SEM image of (a) PMo_{12}-RuO_2 and (b) $PMo_{10}V_2$-RuO_2.

The highly negatively charged POM clusters act as potent structure-directing agents and nucleation centers. During the hydrothermal process, the ruthenium cations (Ru^{3+}) strongly interact with the terminal and bridging oxygen atoms of the POMs via electrostatic attraction and coordination. This strong interfacial binding restricts the continuous, highly crystalline, and anisotropic growth of RuO_2 into large blocks. Instead, the spatial confinement effect of the POM clusters forces the RuO_2 to nucleate and grow into small, low-crystallinity spherical nanoparticles. Furthermore, the strong electrostatic repulsion provided by the high negative charge density of the POMs (especially the V-substituted ones) prevents severe interparticle agglomeration, leading to the well-dispersed spherical morphology observed in our SEM and TEM results.

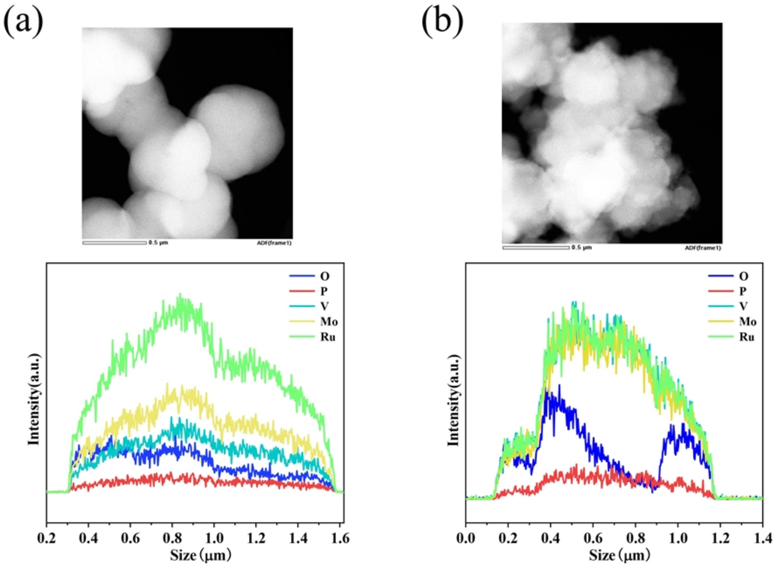

Figure S7. EDS line scan analysis of (a) $PMo_{10}V_2$-RuO_2 and (b) PMo_{12}-RuO_2.

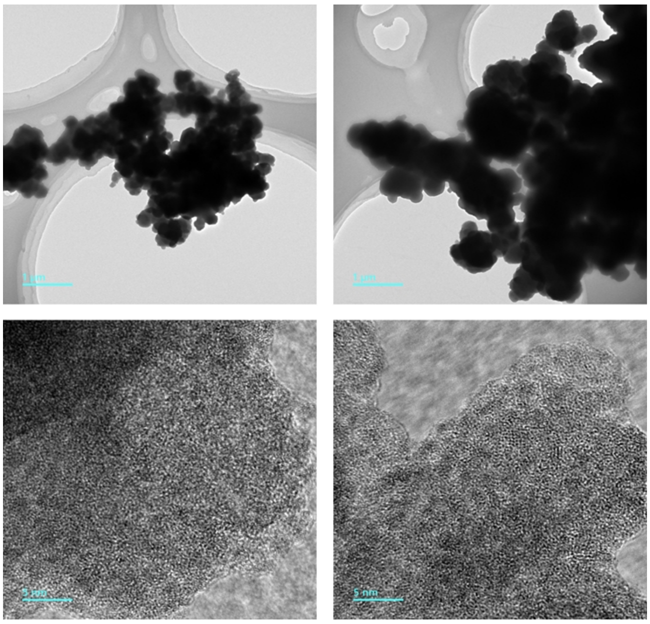

Figure S8. The TEM and HRTEM image of PMo_{12}-RuO_2.

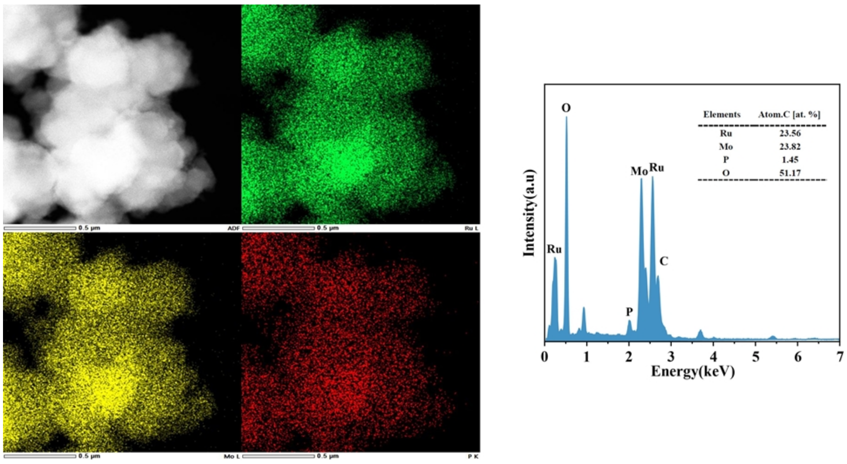

Figure S9. The EDS mapping profile and EDS spectrum of PMo_{12}-RuO_2.

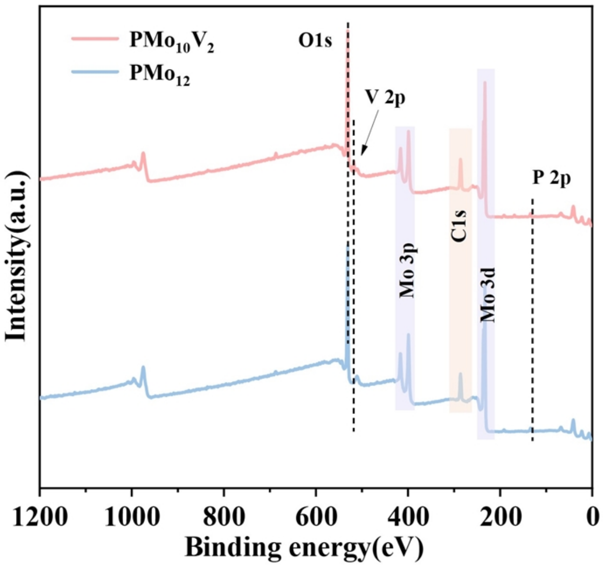

Figure S10. The XPS survey spectra of PMo_{12} and $PMo_{10}V_2$.

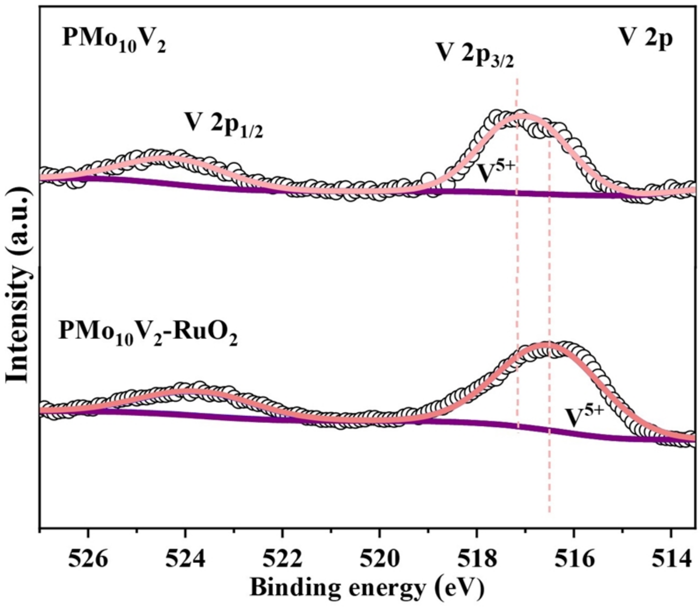

Figure S11. The XPS spectra of V 2p for $PMo_{10}V_2$ and $PMo_{10}V_2$-RuO_2.

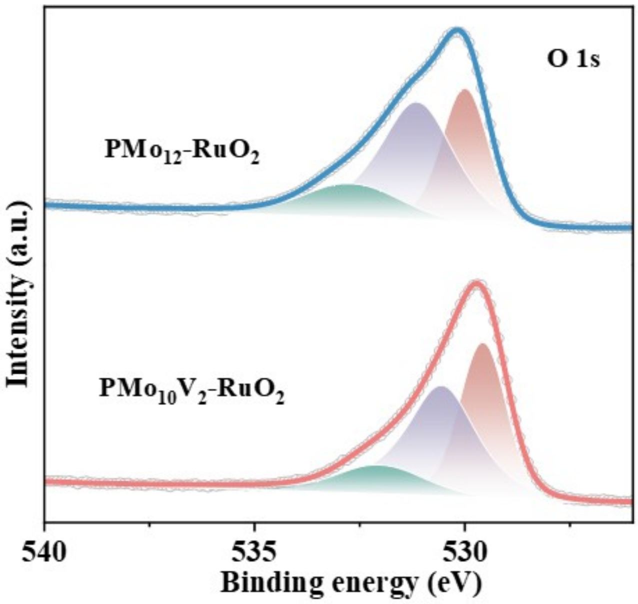

Figure S12. The XPS spectra of O1s for PMo_{12}-RuO_2 and $PMo_{10}V_2$-RuO_2.

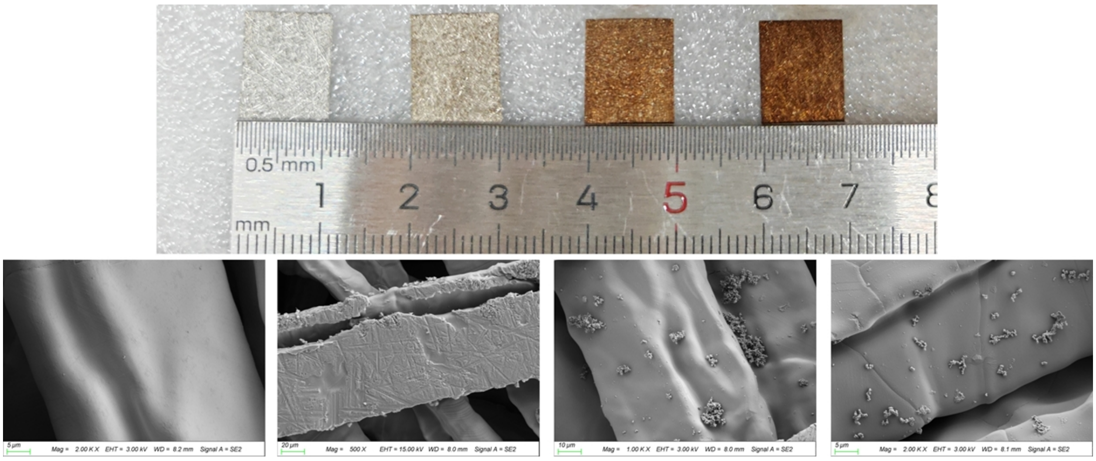

Figure S13. The electronic photographs and corresponding SEM images of the prepared self-supporting materials, from left to right are: pure Ti foam, RuO_2/Ti, PMo_{12}-RuO_2/Ti and $PMo_{10}V_2$-RuO_2/Ti.

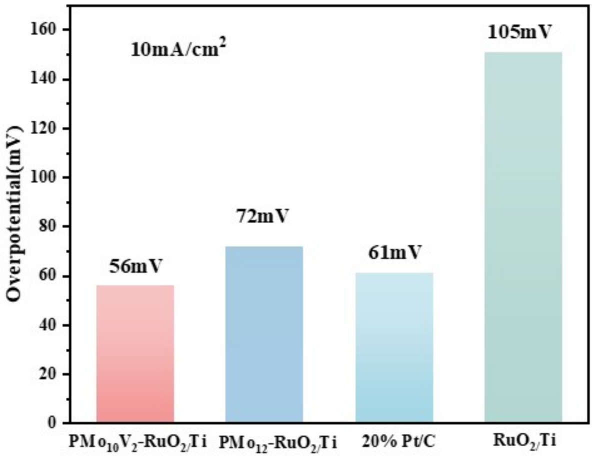

Figure S14. The overpotential at 10 mA/cm^2 of different catalysts.

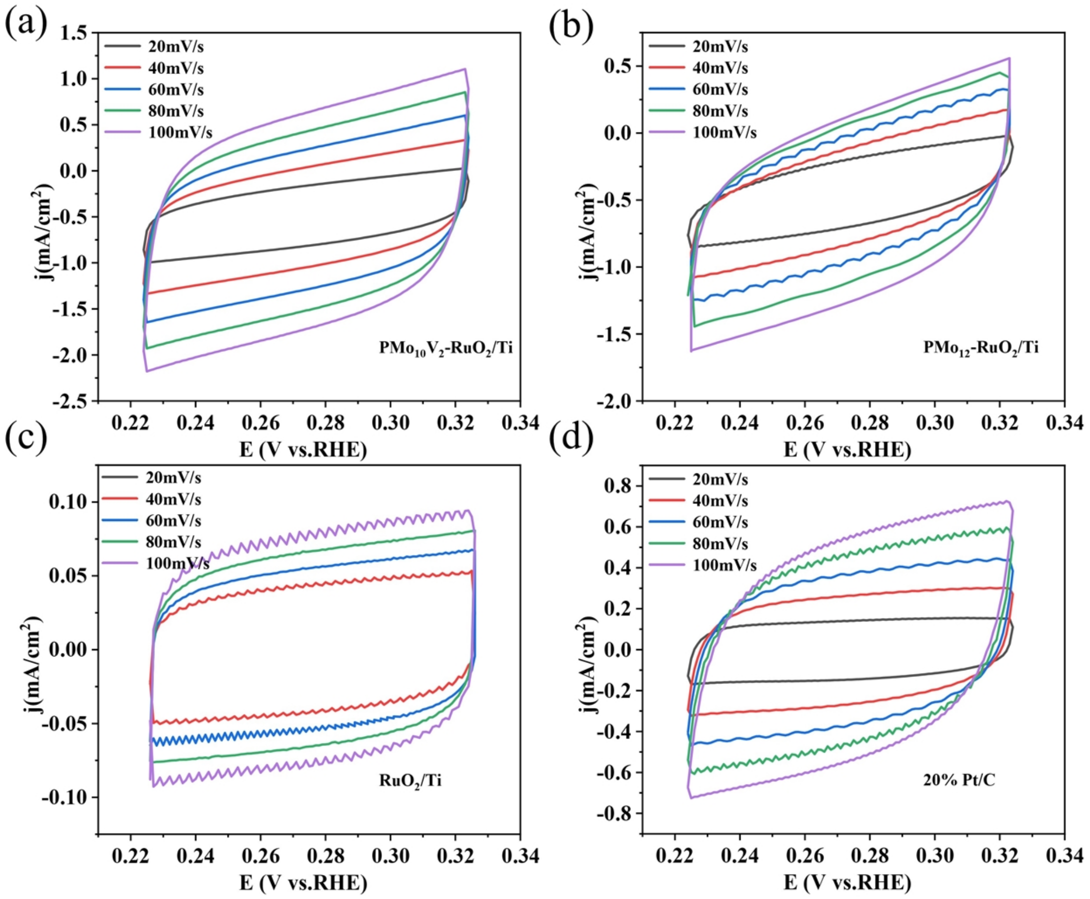

Figure S15. CV profiles of (a) $PMo_{10}V_2$-RuO_2/Ti, (b) PMo_{12}-RuO_2/Ti, (c) 20% Pt/C and (d) RuO_2/Ti catalysts in the non-Faradaic region of 0.22~-0.32 V *vs.* RHE with the scan rates of 20, 40, 60, 80 and 100 mV/s.

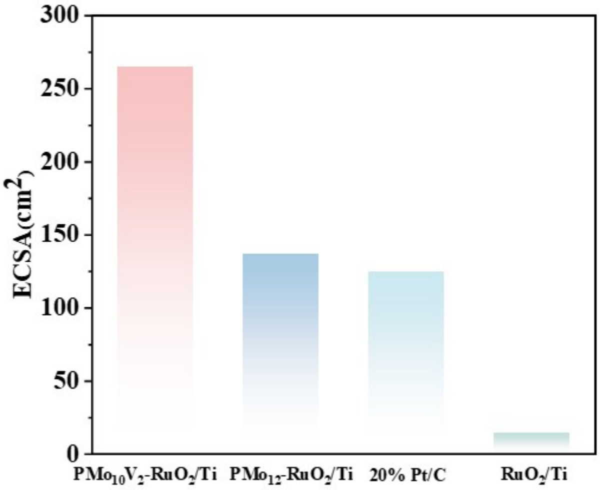

Figure S16. Electrochemically active surface area for different catalysts.

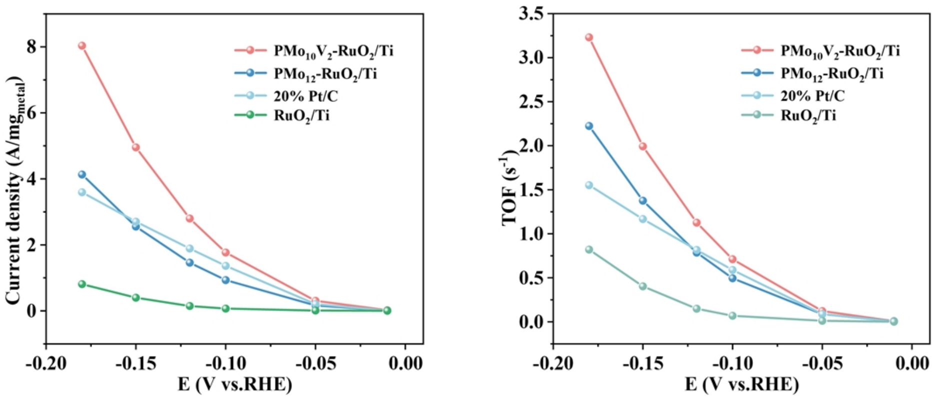

Figure S17. Mass activity and TOF value for catalysts at different potential.

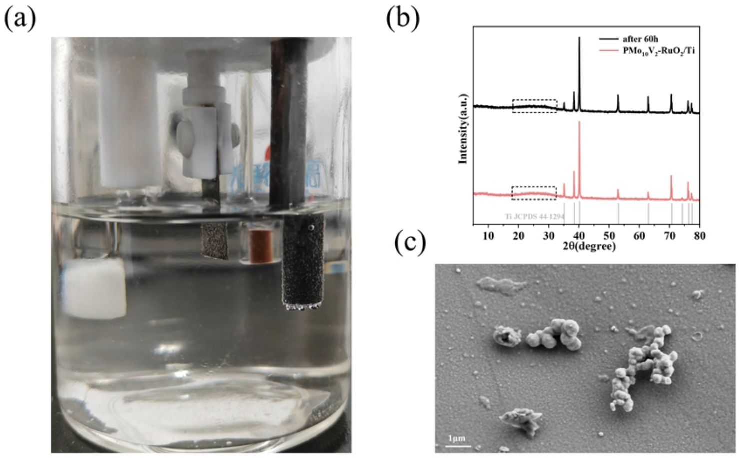

Figure S18. (a) Chronopotentiometry testing process for HER, (b, c) XRD and SEM analysis after 60 h stability test for $PMo_{10}V_2$-RuO_2/Ti.

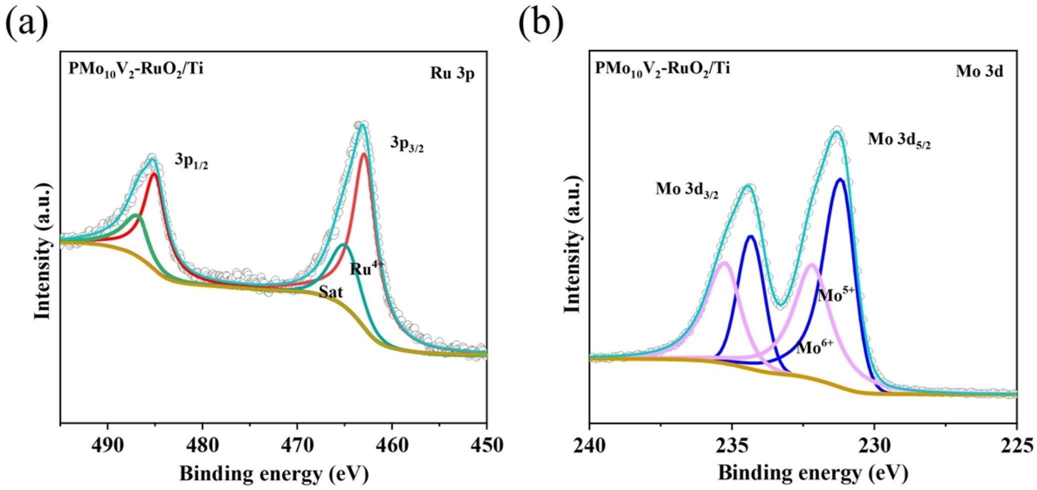

Figure S19. (a) high-resolution Ru 3p XPS spectra; (b) high resolution Mo 3d XPS spectra after after 60 h stability test.

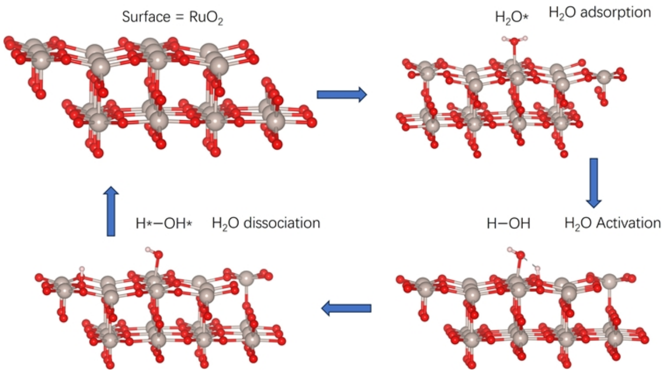

Figure S20. Schematic models of H_2O adsorption, activation and dissociation for RuO_2.

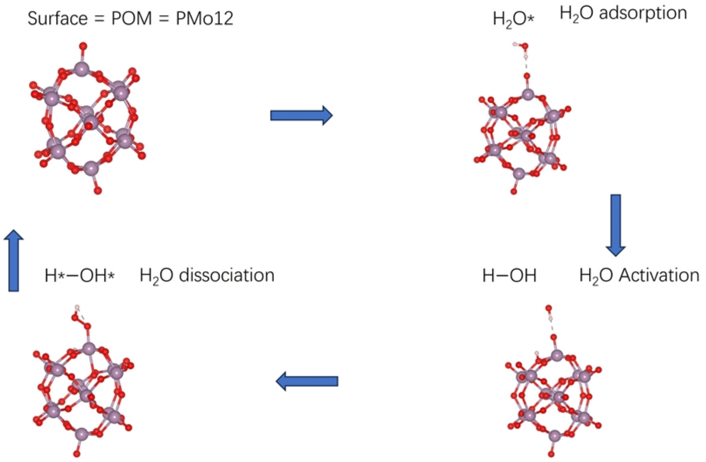

Figure S21. Schematic models of H_2O adsorption, activation and dissociation for PMo_{12}.

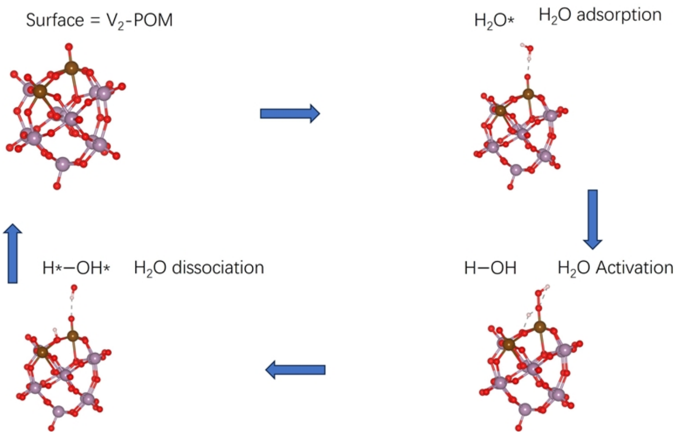

Figure S22. Schematic models of H_2O adsorption, activation and dissociation for $PMo_{10}V_2$.

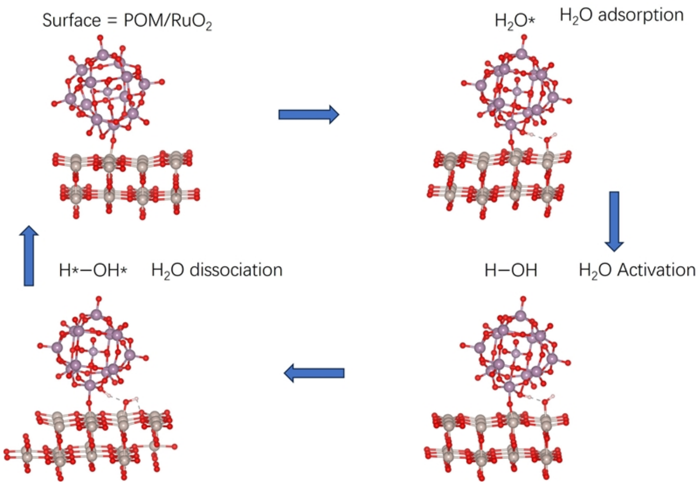

Figure S23. Schematic models of H_2O adsorption, activation and dissociation for PMo_{12}-RuO_2.

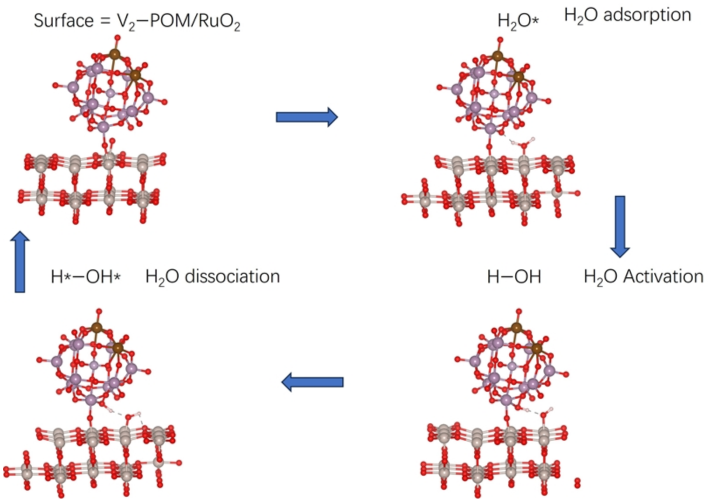

Figure S24. Schematic models of H_2O adsorption, activation and dissociation for $PMo_{10}V_2$-RuO_2.

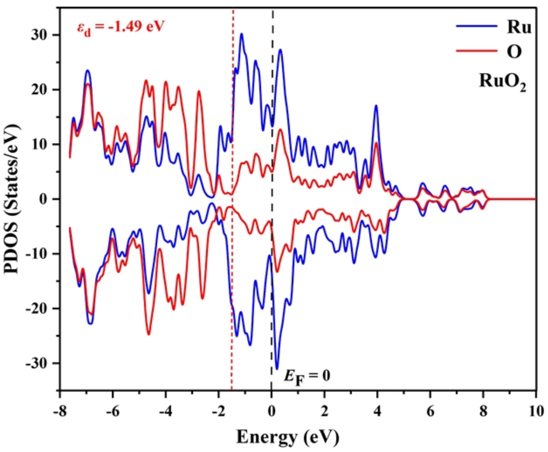

Figure S25. PDOS of RuO_2 sample.

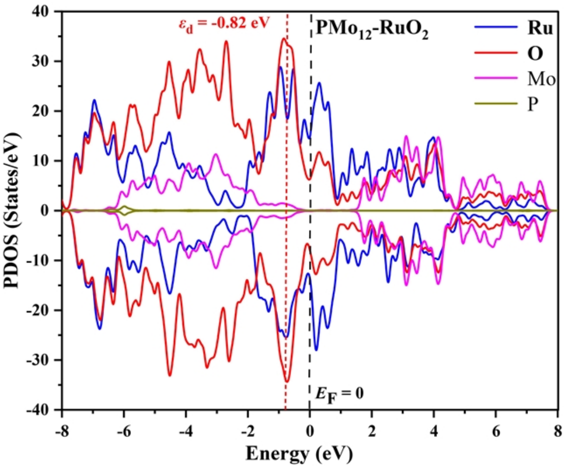

Figure S26. PDOS of PMo_{12}-RuO_2 sample.

(Sample preparation: 1 cm² of the electrode was completely dissolved in aqua regia and diluted to 25 mL for testing.)

Sample	V_0(mL)	Element	Test Solution Concentration (mg/mL)	Dilution Factor	Original Digestion Solution Concentration(mg/mL)
PMo_{12}-RuO_2/Ti	25	Ru	2.7965	10	27.9650
	25	P	0.3458	1	0.3458
	25	Mo	1.2855	10	12.8550
$PMo_{10}V_2$-RuO_2/Ti	25	Ru	2.7048	10	27.0480
	25	P	0.3346	1	0.3346
	25	Mo	1.0378	10	10.3780
	25	V	1.1025	1	1.1025

Table S1. ICP-OES analysis of the in-situ grown catalysts on Ti foam.

References

[1] Kresse G, Furthmüller J. Efficiency of ab-initio total energy calculations for metals and semiconductors using a plane-wave basis set. ***Computational materials science***. **1996**;6:15–50.

[2] Kresse G, Furthmüller J. Efficient iterative schemes for ab initio total-energy calculations using a plane-wave basis set. ***Physical review B***. **1996**;54:11169.

[3] Gajdoš M, Hummer K, Kresse G, Furthmüller J, Bechstedt F. Linear optical properties in the projector-augmented wave methodology. ***Physical Review* B**—*Condensed Matter and Materials Physics.* 2006;73:045112.

[4] Perdew JP, Chevary JA, Vosko SH, Jackson KA, Pederson MR, Singh DJ, et al. Atoms, molecules, solids, and surfaces: Applications of the generalized gradient approximation for exchange and correlation. Physical review B. 1992;46:6671.

[5] Ernzerhof M, Scuseria GE. Assessment of the Perdew–Burke–Ernzerhof exchange-correlation functional. ***The Journal of chemical physics.*** **1999**;110:5029–36.

[6] Sancho-Garcı́a J, Brédas J, Cornil J. Assessment of the reliability of the Perdew–Burke–Ernzerhof functionals in the determination of torsional potentials in π-conjugated molecules. ***Chemical physics letters.*** **2003**;377:63–8.

[7] Grimme S, Ehrlich S, Goerigk L. Effect of the damping function in dispersion corrected density functional theory. ***J Comput Chem.*** **2011;**32:1456–65.

[8] Li W, Kong L, Chen C, Gou J, Sheng S, Zhang W, et al. Experimental realization of honeycomb borophene. ***Science Bulletin.*** **2018**;63:282–6.

[9] Yu M, Trinkle DR. Accurate and efficient algorithm for Bader charge integration. ***The Journal of chemical physics*. 2011**;134.